LOCAL HEAT TRANSFER COEFFICIENT DISTRIBUTION OF AIR ROUND JET FLOWING INSIDE A CYLINDRICAL CAVITY

Mataoui Amina* and Zidouni-Kendil Faiza**
*Laboratoire de Mécanique des Fluides Théorique et Appliquée
Faculté de Physique
Université des sciences et de la technologie Houari Boumediene
B.P. 32, Bab Ezzouar, 16111 Al Alia, Alger, Algérie
e-mail : mataoui_amina@yahoo.fr
**Centre de Recherche Nucléaire de Birine, COMENA, BP 180 Ain Oussara, Djelfa, ALGERIE

ABSTRACT - The present study aims to conduct a numerical investigation of dynamical and thermal round jet behaviour while evolving into a cylindrical cavity. Steady-state simulations were performed and the flow was considered incompressible and fully turbulent. The numerical method solves both the steady Reynolds averaged Navier –Stokes equations (RANS) and the continuity equation in an incompressible fluid. The closure of the flow equations system is achieved using a one-scale energy- dissipation model at high Reynolds number coupled with a wall function treatment in the vicinity of the wall boundaries.. A very steep gradient of variables prevails in viscous sublayer so to properly resolve the flow in the region sufficiently fine grid is managed. Because the thermal and dynamic aspect can not be dissociated in such flow configuration, we have undertaken the both aspects to examine the effect of the impinging distance, the velocity, turbulent characteristics on the Nusselt number. So the Reynolds numbers is ranged between 22 000 and 50 000. The distance between the jet exit and the bottom wall L_f is varied from 2 to 30 jet diameters. It is found that the variations of the Nusselt number on the stagnation point can be correlated by power laws of the form $Nu = CRe^n$. For the same Reynolds number, the heat transfer intensity of the bottom surface is much higher than that of the lateral surface with increasing L_f/d and the distribution of the local heat transfer coefficient on the lateral surface is similar to that on a flat plate over which a fluid flows. The Nusselt numbers for the bottom and the lateral surfaces increase first, reach their maxima and then decrease. The maximum Nusselt number occurs for the case $L_f/d=8$ and the initial turbulence rate has not a significant effect on the Nusselt Number evolution. These results of thermal transfer are compatible with the dynamic structure which developed inside the cavity and emphasize a good precision of calculation by comparison with the experimental data and numerical prediction of several researchers.

Key-Words: - Jet impingement - turbulence model - Wall function - Nusselt Number

1 INTRODUCTION

Impinging jet is a well-known technique for enhancing heat transfer between a fluid and a surface. A review of the literature revealed that many of the published work deals with impinging jets onto different types of surfaces particularly for heat exchange studies[1], [2], [3], [4], [8]. It is widely utilized in many industrial processes. Such as drying, annealing, tempering, curing and cooling of surfaces that are exposed to high heat flux. Taking the tempering process of glassware as an example, after being formed in a metal model, a glass work piece is rapidly cooled by multiple air jets. The process is usually completed in several minutes during which the temperature drop may be as large as about 400- 5000 °C. A well-organized cooling system is the key to achieve high productivity. A poor cooling system causes an unfavourable distribution of internal stress which may give rise to cracking work piece. The adjustment of the local heat transfer rate is carried out by the control of flow rate, location and dimension of the jet nozzle. In order to obtain a reasonable distribution of the local heat transfer rate, an understanding of the heat transfer characteristics (especially the local behaviour) of the impinge jet is of great importance in glass tempering problem. Across the broad spectrum of applications, a variety of impingement surfaces is employed. The particular surface to be investigated in the present paper

is the surface of a cylindrical cavity with its one end open to the ambient air. A round nozzle is situated at its axis. This configuration is often encountered in the tempering of glassware and the coaling of electronic equipment. A schematic diagram of the investigated configuration is shown in figure1.
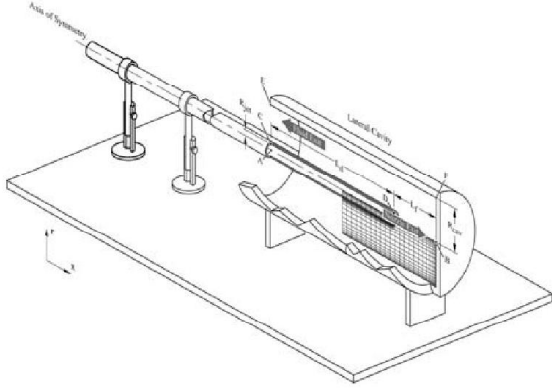

Figure 1: *Geometry and computational domain L_f=8d*

2 Turbulence Model

The considered fluid is assumed Newtonian and incompressible with constant physical properties. The flow was stationary. The aerodynamic field is described by the conservation equations of mass and momentum expressed by the averages of Reynolds of their corresponding equations:

$$\frac{\partial U_i}{\partial x_i} = 0 \tag{1}$$

$$U_j \frac{\partial U_i}{\partial x_j} = -\frac{\partial}{\partial x_i}\left(\frac{P}{\rho}\right) + \frac{\partial}{\partial x_j}\left(\nu \frac{\partial U_i}{\partial x_j} - \overline{u_i u_j}\right) \tag{2}$$

$$U_j \frac{\partial T}{\partial x_j} = \frac{\partial}{\partial x_j}\left(\alpha \frac{\partial T}{\partial x_j} - \overline{u_j\theta}\right) \tag{3}$$

The standard k-ε model of Jones and Launder (1972) [5], based on the concept of Prandtl-Kolmogorov's turbulent viscosity was used in its high Reynolds number form. It is based on the concept of turbulent eddy viscosity and turbulent Reynolds stress tensor is obtained by algebraic constitutive low:

$$\begin{cases} \overline{u_i u_j} = \frac{2}{3}k\delta_{ij} - \nu_t(U_{i,j} + U_{j,i}) \quad \text{et} \quad \overline{u_j\theta} = \Gamma_t \frac{\partial T}{\partial x_j} \\ \nu_t = C_\mu \frac{k^{3/2}}{\varepsilon} \qquad \text{et} \quad \Gamma_t = \frac{\nu_t}{Pr_t} \end{cases} \tag{4}$$

The turbulence field is then obtained by solving the modelled equation of k and ε

$$U_j k_{,j} = \nu_t\left(U_{i,j} + U_{j,i}\right)U_{i,j} + \left[\left(\nu + \frac{\nu_t}{\sigma_k}\right)k_{,j}\right]_{,j} - \varepsilon \tag{5}$$

$$U_j\varepsilon_{,j} = c_{\varepsilon 1}\nu_t\frac{\varepsilon}{k}\left(U_{i,j} + U_{j,i}\right)U_{i,j} - \\ c_{\varepsilon 2}\frac{\varepsilon^2}{k} + \left[\left(\nu + \frac{\nu_t}{\sigma_t}\right)\varepsilon_{,j}\right]_{,j} \tag{6}$$

The molecular diffusion terms were negligible in the present application provided that the near wall region was not considered. The value of $\sigma_{\varepsilon,t}$ was deduced from the value of the velocity profile slope in a logarithmic boundary layer with a von Karman constant κ=0.41 using the relation:

$$\sigma_{\varepsilon t} = \frac{\kappa^2}{C_\mu^{\frac{1}{2}}\left(C_{\varepsilon 2} - C_{\varepsilon 1}\right)} \tag{7}$$

As usual in all one point closures, a single length scale l =$k^{2/3}/\varepsilon$ was used in all the model hypotheses. So the k-ε model will be referred to as single-scale model. The physical significance is this assumption of an implicit spectral self-similarity which is imbedded in one point closures.

The numerical constants are given in Table 1.

C_μ	$C_{\varepsilon 1}$	$C_{\varepsilon 2}$	$\sigma_{k,L}$	$\sigma_{k,t}$	$\sigma_{\varepsilon,t}$
0.09	1.44	1.92	1.0	1.0	1.3

Table 1: *Numerical constants for the k-ε model*

3 Wall Function Approach

The standard k-ε model of Jones and Launder (1972) based on the concept of Prandtl-Kolmogorov's turbulent viscosity was used in its high Reynolds number form. The wall treatment boundary conditions were achieved using the wall function technique of Launder and Spalding (1974) that bridges the viscosity affected region (viscous sub-layer) between the wall and the fully turbulent region.
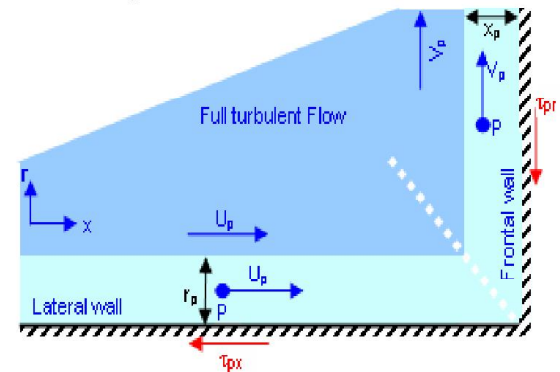

Figure 2 : *Near wall treatment*

The dimensionless variables, Figure 2, of distance and velocity are defined as:
Along the lateral walls:

$$U_p^+ = \frac{U_p}{U_t} \; ; \; r_p^+ = \frac{\rho U_t r_p}{\mu} \tag{8}$$

Where : $U_\tau = \sqrt{\dfrac{\tau_{px}}{\rho}}$ and $\tau_{px} = \rho \dfrac{C_p^{1/4} k_p^{1/2} U_p}{U_p^+}$

Along the frontal wall:

$$V_p^+ = \frac{V_p}{V_\tau} \; ; \; x_p^+ = \frac{\rho V_\tau x_p}{\mu} \tag{9}$$

Where $V_\tau = \sqrt{\dfrac{\tau_{pr}}{\rho}}$ and $\tau_{pr} = \rho \dfrac{C_p^{1/4} k_p^{1/2} V_p}{V_p^+}$

k_p is the turbulent kinetic energy at the first grid point near the wall.

4 Computational Parameters
4.1 Geometry and Grid Arrangement

The geometrical conditions are specified in Figure 1. The turbulent air flow at the exit of the nozzle, with diameter d=2r_{jet}, was fully developed. The length used for the pipe was L_t=24d for all configurations to assume the well developed flow. The nozzle diameter d was 3.7 cm. The radius of the cavity R_{cav} which delimits the computational domain was equal to 3.94d.

The computational domain and mesh are shown in Figure 3. The grid contains 100*36 points for an 8d configuration starting upstream of the jet duct. This configuration was used to check the validity of the calculations to experiments data carried out by A. Benaissa (1985) [3]. Such a grid showed good agreement with the experimental results. There were 60*36 cells before the nozzle exit which corresponded to 900mm of the jet duct. A refinement before and after the nozzle exit was applied so that the entrainment was accurately described. In the radial direction, 6 cells lay within the jet duct pipe. The grid was refined near the symmetry axis (in order to have sufficient accuracy near the stagnation point and at the edge of the nozzle. A sufficiently fine grid was managed near the cavity and duct walls because a very high gradient of variables prevailed in the viscous sub-layer. The radial and axial grid stretching (coarse meshes) was applied elsewhere far from the walls. All results were independent by refining the grid in the two directions.

The different grids used when changing the distance from the exit nozzle to the end of cavity are shown below.

Configurations	4d	8d	10d	15d	20d	25d	30d
Grid size	80 x 36	100 x 36	110 x 36	135 x 36	160 x 36	185 x 36	210 x 36

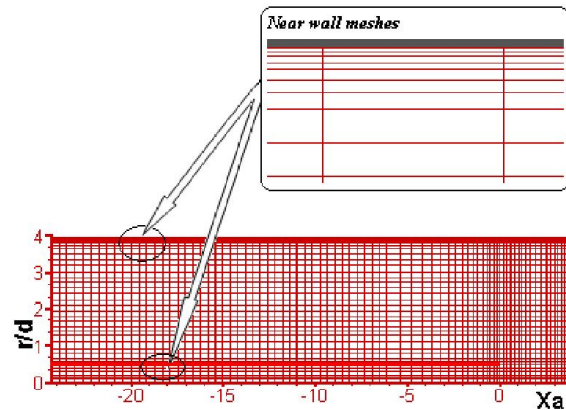***Table 2:*** *Grid and mesh sizes for the studied configurations.*

Figure 3 : *Grid arrangement for configuration L_f=4d*

4.2 Boundary Conditions
Four boundaries conditions were used in this numerical prediction. The flow field within the computational domain are as follow:

4.2.1 Air jet duct inlet
The condition in the inlet jet duct (boundary AC in fig. 1) is important in predicting the center line velocity and shear stress. The velocity profile at the nozzle exit is affected by the nozzle design such as the length-to-diameter ratio and the nozzle shape. In this paper a uniform velocity profile was considered. The mean and turbulent quantities at the inlet imposed are described by:

$$U=U_i, \quad \text{and } V=0, \tag{10}$$
$$\alpha = 10^{-4} U_i^2, \tag{11}$$
$$\varepsilon_i = \alpha^{1.5}/0.15d, \tag{12}$$

4.2.2 The wall surfaces
The wall boundary conditions CD, EF and BF (fig.1.) were used at used at the solid wall of the cavity and duct. The no-slip boundary conditions were imposed.

For the evaluation of the wall effect on turbulence, the wall-function and near wall modelling (Launder and Spalding 1974) approaches have been used to model the wall bounded turbulent flow. The semi-empirical formulas are used to bridge the viscosity affected region (viscous sublayer and buffer layer) between the wall and the fully turbulent region.

4.2.3 Air exit boundary
The boundary CF in (Fig.1.) is the air exit boundary. The OUTFLOW (fully developed) boundary conditions were used. For the OUTFLOW boundary conditions, the velocity gradients and turbulent quantities across this boundary were set to zero., the relative static pressure is assumed to be equal to the atmospheric pressure.

$$\left.\frac{\partial V}{\partial x}\right|_{x-0} = \left.\frac{\partial k}{\partial x}\right|_{x-0} = \left.\frac{\partial \varepsilon}{\partial x}\right|_{x-0} = 0 \tag{13}$$

4.2.4 Axis of symmetry

The axis boundary conditions were used along the center line (AB) in figure1. The radial velocity component V and the gradient of the other dependent variables were equal to zero

$$V = 0$$

$$\left.\frac{\partial U}{\partial r}\right|_{r=0} = \left.\frac{\partial k}{\partial r}\right|_{r=0} = \left.\frac{\partial \varepsilon}{\partial r}\right|_{r=0} = 0 \qquad (14)$$

4.3. Modelling Parameters

Numerical values for mean parameters used in different computational simulations are given in Table 3. Parameter of the validation case, were selected according experiments for configuration L_f=8d. For the numerical prediction cases, the parameters used to investigate is the influence of impinging distance L_f on the flow characteristics specially the centreline static pressure and the skin friction at the cavity walls. All the numerical simulations were carried out at ambient pressure.

D_{cav}	D_{jet}	L_d	L_f/d	Re
29cm	3.7cm	24	$2 \leq L_f \leq 30$	$20000 \leq Re \leq 100000$

Table 3: Summary of the simulation conditions

5 Numerical Procedure and Computational Methodology

The governing differential transport equations, put in form of Equation 15, were transformed to algebraic equations before being solved numerically. In axisymmetric cylindrical coordinates, this equation can be written as equation 16. The finite volume scheme of S. Patankar (1980) [7], which involved integrating the governing equation about each control volume, yielding discrete equations that conserve each quantity on a control-volume basis was applied to Equation 15.

$$\text{div}\left(\rho U \Phi\right) = \text{div}\left(\Gamma_\Phi \text{grad}\Phi\right) + S_\Phi \qquad (15)$$

$$\frac{1}{r}\left(\frac{\partial}{\partial x}(r\rho U\Phi) + \frac{\partial}{\partial r}(r\rho V\Phi)\right) =$$
$$\frac{1}{r}\left(\frac{\partial}{\partial x}\left(r\Gamma_\Phi \frac{\partial \Phi}{\partial x}\right) + \frac{\partial}{\partial r}\left(r\Gamma_\Phi \frac{\partial \Phi}{\partial r}\right)\right) + S_\Phi \qquad (16)$$

Where the 'scalar' variableΦ, the diffusion coefficient Γ_Φ and source term S_Φ in the respective governing equation are given in Table 4.

Cont.	Φ	Γ_Φ	S_Φ
r moment	U	μ_{eff}	$-\frac{\partial P}{\partial r} + \frac{\partial}{\partial x}\left(\mu_{eff}\frac{\partial U}{\partial r}\right) + \frac{1}{r}\frac{\partial}{\partial r}\left(r\mu_{eff}\frac{\partial V}{\partial r}\right) - 2\mu_{eff}\frac{V}{r^2}$
x moment	V	μ_{eff}	$-\frac{\partial P}{\partial x} + \frac{\partial}{\partial x}\left(\mu_{eff}\frac{\partial U}{\partial x}\right) + \frac{1}{r}\frac{\partial}{\partial r}\left(r\mu_{eff}\frac{\partial V}{\partial x}\right)$
k equation	K	$\mu + \frac{\mu_t}{\sigma_k}$	$G - \rho\varepsilon$
ε equation	ε	$\mu + \frac{\mu_t}{\sigma_\varepsilon}$	$C_{\varepsilon 1}\frac{\varepsilon}{k}G - \rho\frac{\varepsilon^2}{k}$

Table 4: *Diffusion Coefficient and Source terms in the generic transport Equation (6)*

$$\mu_{eff} = \mu + \mu_t \qquad ;$$

$$\mu_t = C_\mu \rho \frac{k^2}{\varepsilon}$$

$$G = \mu_t\left[\left(\frac{\partial U}{\partial r} + \frac{\partial V}{\partial x}\right)^2 + 2\left(\frac{\partial U}{\partial x}\right)^2 + 2\left(\frac{\partial V}{\partial r}\right)^2 + 2\left(\frac{V}{r}\right)^2\right]$$

C_μ, $C_{\varepsilon 1}$, $C_{\varepsilon 2}$, $\sigma_{k,l}$ and $\sigma_{k,t}$ are specified in Table 1.

These equations were discretised using the second order upwind scheme to achieve best accuracy. The interpolation scheme (PLDS) was used with the staggered meshes, Figure 5. Pressure-velocity coupling was achieved using the SIMPLE (Semi-Implicit Method for Pressure-Linked Equations) algorithm. The governing equations were solved using the T.E.A.M code [7].

6 Results and Discussions

6.1 Dynamic Field description

Figure 4 shows the evolution of the developed eddies in the cavity for different impinging distances at Re=20 000, 50 000, 100 000. At a short impinging distance 2d< L_f <8d, the principal jet strikes the frontal wall and returns towards the exit of the cavity. The exit flow is divided into two parts:
1. A first part leaves the cavity at low speed
2. The second part was aspired by the jet by giving rise to a steady toroidal eddy (swirl) at the bottom of the cavity. This zone is characterized by a low mean velocity, an important turbulent energy and a negative pressure due to the Coanda effect , Mataoui A. (2000) [8]. The principal jet is also narrowed. When L_f> 4d, the centre of this eddy remained motionless when the impinging distance increased.

From the impinging distance L_f>10d, Figures 4, a contra rotating secondary eddy appeared at the bottom of the cavity. The mean velocity of this secondary swirl was very weak. Its dimension grew gradually when the distance L_f increased. Its maximum velocity was attained for L_f=28d. At L_f> 20d (Figure 4), a third eddy appeared at the bottom of the cavity with a very low speed. It reached its maximum size with L_f = 28d. In this case, a fourth swirl with an irregular form and infinitesimal speed appeared. This one tended to be stretched in the horizontal direction.

For all examined impact distances, we observed a small eddy around the jet duct which is due to a negative pressure around the duct. This is confirmed by Benaissa A. (1985) [3]. He observed around the jet a black net carbon smoke used for visualization returning in the cavity. This is due to an aspiration of the external fluid creating a small swirl on the external wall of the jet duct.
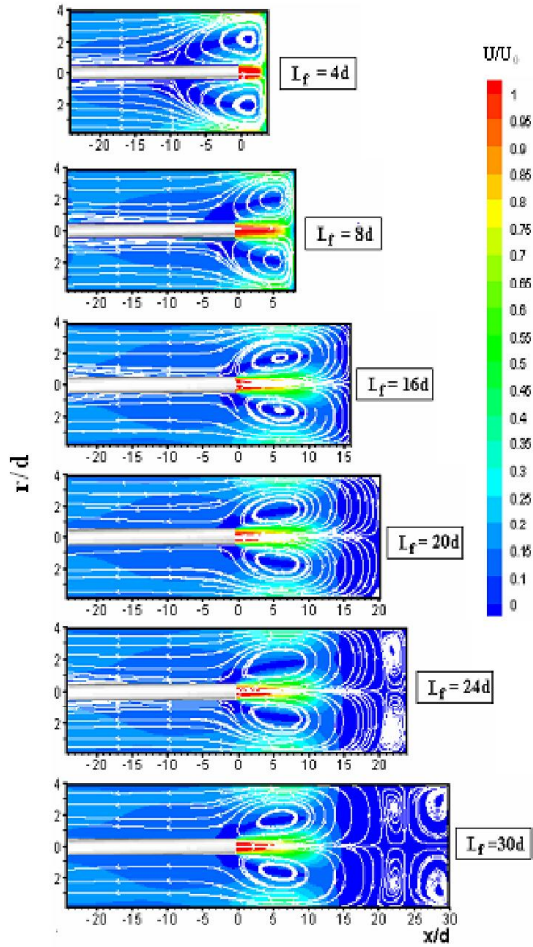
Figure 4: *Velocity contours plots in the cavity at variable L_f (Re=20 000, 50 000, 100 000).*

6.2 Thermal Field description

2.1.1 Evolution of Nusselt number with the Flow characteristics

$$\text{Nu}_F = \frac{L|q_{wF}|}{\lambda(T_w - T_0)} \quad ; \quad \text{Nu}_L = \frac{L|q_{wL}|}{\lambda(T_w - T_0)} \quad (17)$$

$$\text{With} \quad q_{wF} = -\lambda\left(\frac{\partial T}{\partial x}\right)_{x_p} \quad ; q_{wL} = -\lambda\left(\frac{\partial T}{\partial r}\right)_{r_p} \quad (18)$$

The lateral and frontal cavity walls Nusselt number distribution is studied for several impact distances from the exit jet to the bottom of the cavity.

At the same Reynolds number, the heat transfer intensity of the bottom surface is much higher than that of the lateral surface, see figures below.
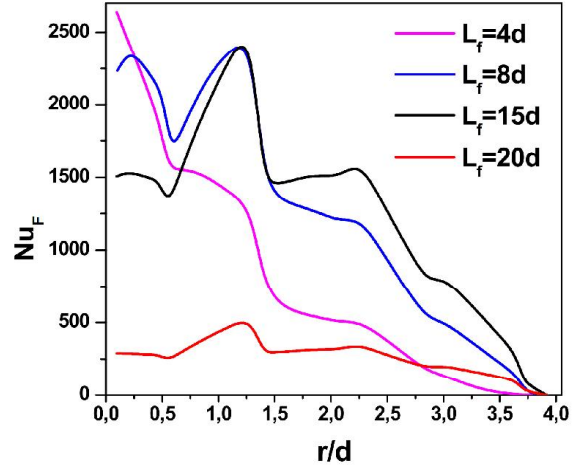
a. Influence of the impinging distance

Figure 5a : *Nusselt Number on the frontal wall at different impinging distance*

In figure5a, the first peak (maximum Nusselt number) corresponds to the stagnation point and decrease to r=0.5d which corresponds to the section jet this maximum is due to the existence of a quasi uniform a velocity profile around the stagnation point. For a more important impinging distance, this maximum disappears because of the attenuation of the jet, see figure 4. The second peak around r=1.4d, corresponds to the development of a wall jet on the frontal cavity wall. These first two peaks were also noticed by Merci B (2003), in their study of a turbulent axisymmetric jet impacting a plane plate. Merci B noticed the second peak location around r=2d from the axis of the jet. This discrepancy from our case can be explained by the presence of lateral wall which confines wall jet and reduce its section.

Figure 5b : *Nusselt Number on the Lateral wall at different impinging distances*

In figure 6a and 6b, we can observe that an increasing of Reynolds number causes a systematic increasing of the Nusselt number, this is well revisable.
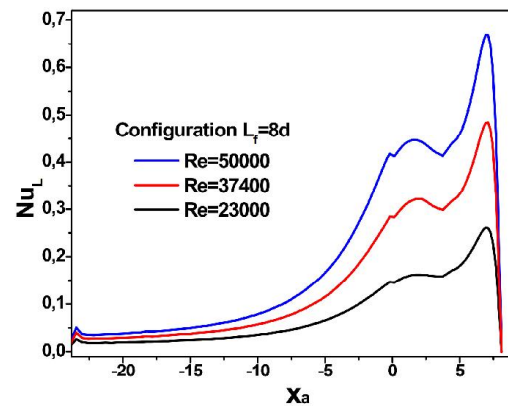

Figure 6a : *Nusselt Number on the Lateral wall at different Reynolds number*

On the side wall, figure 5b, for impinging distance L_f ≤ 8d, we observe two peaks: The first peak is located at the section x=-5d for L_f=4d and at the section x=0 for L_f=8d.The second peak is located at x=2.5d for the L_f=4d and x=0 for the L_f=8d. When L_f ≥ 15d, the evolution contain only one peak at the section x=10d.

The distribution of the local heat transfer coefficient on the lateral surface is similar to that on a flat plate over which a fluid flows this is also found by Hai-jun Kang (1989).
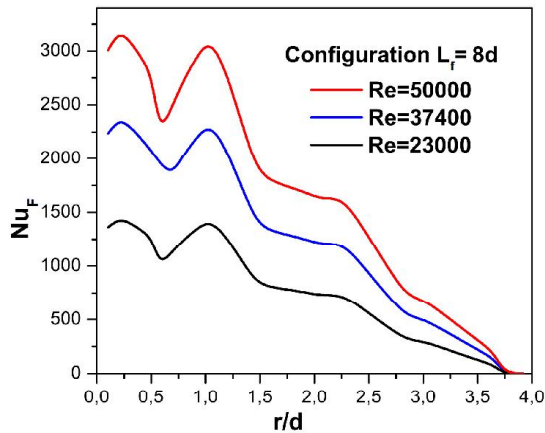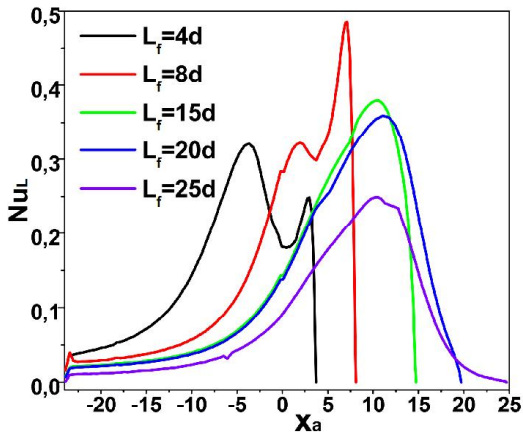

Figure 6b: *Nusselt Number on the frontal wall at different Reynolds number*

The bibliography survey highlighted the importance of the turbulence generated by the jet on the characteristics of transfer of heat on the impinging walls. We can note that certain authors justified the variation of their results compared to the others is due to imprecision of that initial turbulence rate R.S.Amano (1984) [2] & [8].

We examined this effect on the fontal and lateral cavity wall. The curves are slightly different even the evolution profile is the same. So we can conclude that the rate of initial turbulence is a significant parameter especially on the frontal wall. Its influence on the side wall is somewhat negligible, this is well confirmed by Risso F. (1997)[11] .
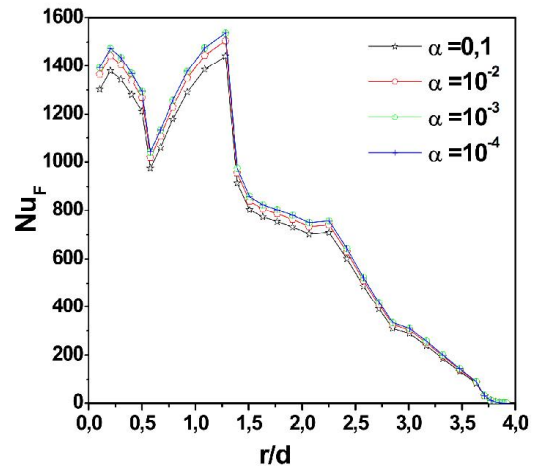

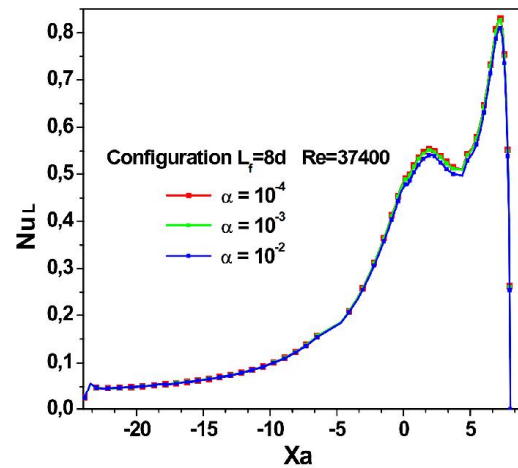**Figure 7a** *: Nusselt Number Evolution with Initial turbulence intensity on the frontal wall*

Figure 7b *: Nusselt Number Evolution with Initial Turbulence Intensity on the Lateral wall*
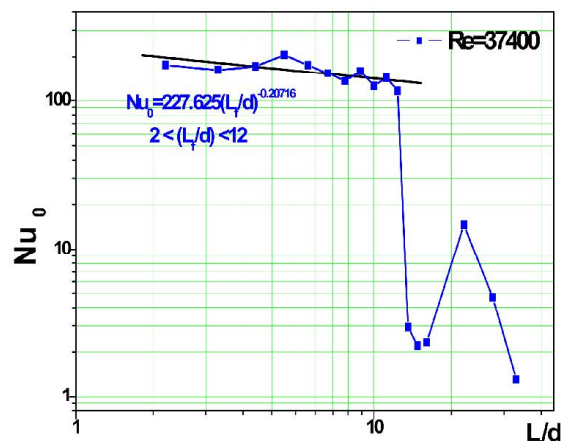

Figure 8: *Correlation of Nusselt number at the stagnation point*

Finally a good correlation of Nusselt number at the stagnation point for a fixed Reynolds number (Re= 37400) between the impinging distance (L_f) and the nozzle jet exit diameter (d), is found, figure 8 . For the impingement distance $2<L_f<12$ the correlation is expressed by the following relation:

$$Nu_0 = 27,625 \left(\frac{L_f}{d} \right)^{-0,207}$$

7 Conclusion

The heat transfer and dynamic behaviour of a turbulent axisymmetric jet flowing into a cylindrical cavity has been modelled numerically. A parametrical study has been made by varying the distance between the jet exit and the bottom surface of the cavity and varying the Reynolds numbers.

This study allowed us to deduce these points:

- The Nusselt number at the stagnation point can be correlated by power laws of the form $Nu = CRe^n$.
- At the same Reynolds number, the heat transfer intensity of the bottom surface is much higher than that of the lateral surface with increasing L_f/d.
- Nusselt numbers for the bottom and the lateral surfaces increase first, reach their maxima and then decrease.
- The maximum Nusselt number occurs at $L_f/d=8$.
- The local heat transfer coefficient, for the bottom surface, decrease with the increase in radius.
- The distribution of the local heat transfer coefficient on the lateral surface is similar to that on a flat plate over which a fluid flows.

References:

[1] Al-aqal O. M. A. (2003). Heat transfer distributions on the walls of narrow channel with jet impingement and cross flow. Dissertation, Engineering science, University of Pittsburgh (2003).

[2] Amano R.S., Brant H. (1984). Numerical Study of Turbulent Axisymmetric Jets Impinging on a Plate and Flowing into an Axisymmetric Cavity. *Journal of Fluid Engineering, 106*, 410-417.

[3] Benaissa A. « Contribution à l'étude de l'évolution d'un jet d'air à symétrie axiale dans une cavité cylindrique », Thèse de Magister, Mécanique des Fluides, USTHB, Alger, Sept. (1985).

[4] Jachna S. (1978). Axisymmetric air jet impingement on a spherical concave plate. Dissertation, Engineering science, NJITH ETD : The New Jersey Institute of Technology's electronic Theses and Dissertations

[5] Jones, W.P., Launder, B.E. (1972). The Prediction of Laminarization with a Two Equation Model of Turbulence. *Int. J. Heat Mass Transfer, 15*, 301-314.

[6] Hai-jun Kang & Wen-Quan Tao « Heat and mass transfer for jet impingement in a cylindrical cavity with one end open to the ambiant air », AIAA Paper 89 – 0173, (1989).

[7] Huang P. G., Leschziner M. A., « An introduction and guide to the Computer Code TEAM », Report TFD/83/9 (R), Thermofluids Division Dept. Mech. Eng., UMIST, (1983).

[8] Mataoui A., Schiestel R. & Salem A., « Application du modèle énergie flux multi-échelles à un jet axisymétrique frappant perpendiculairement une paroi », CD ROM CFD2K- and Proceeding of the 8th annual conférence of the society of Canada, CFD2K , Editor : D . PELLETIER, pp.377-380, Montreal, Quebec, Canada, June 11-13, (2000).

[9] Merci B., De Langhe C., Lodefier K., « Axisymmetric impingement heat transfer with a non linear k-epsilon model », Journal of Themophysics and heat Heat Transfer 18 (1): pp. 100-107, Janv-Mars(2004).

[10] Patankar, S.V. (1980). *Numerical Heat Transfer and Fluid Flow*. McGraw Hill, New York.

[11] Risso, F. and Fabre, J. (1997). Diffusive Turbulence in a Confined Jet Experiment. *J. Fluid Mech. 337*, 233-261.